CHIRAL MATERIALS

Bright, circularly polarized black-body radiation from twisted nanocarbon filaments

Jun Lu[1,2,3], Hong Ju Jung[1,2,3], Ji-Young Kim[1,2,3,4], Nicholas A. Kotov[1,2,3,5]*

Planck's law ignores but does not prohibit black-body radiation (BBR) from being circularly polarized. BBR from nanostructured filaments with twisted geometry from nanocarbon or metal has strong ellipticity from 500 to 3000 nanometers. The submicrometer-scale chirality of these filaments satisfies the dimensionality requirements imposed by fluctuation-dissipation theorem and requires symmetry breaking in absorptivity and emissivity according to Kirchhoff's law. The resulting BBR shows emission anisotropy and brightness exceeding those of conventional chiral photon emitters by factors of 10 to 100. The helical structure of these filaments enables precise spectral tuning of the chiral emission, which can be modeled using electromagnetic principles and chirality metrics. Encapsulating nanocarbon filaments in refractive ceramics produces highly efficient, adjustable, and durable chiral emitters capable of functioning at extreme temperatures previously considered unattainable.

Nanostructured materials can be designed to impart strong ellipticity to propagating photons (*1*–*3*). The rapid development of nanometer-scale photonics (*4*, *5*) and chiral photo- and electroluminescent materials (*6*, *7*) has led to the development of at-source circularly polarized light (CPL) emitters. However, synthesizing chiral molecules, polymers, and crystals that can emit highly intense and strongly polarized light has been challenging. Progress has been made for visible wavelengths (*8*, *9*), but these materials often rely on rare earth metals, raising sustainability issues. For the near-infrared (NIR) devices operating in water transparency windows at 800 and 1550 nm, strong CPL emitters are needed for emergent telecommunication devices (*10*), encrypted networks (*11*), through-space communications (*12*), robotic vision systems (*13*), quantum optical computing (*14*), personalized biomedical technologies (*15*), and biopolymer sensors (*16*). However, the close proximity of vibronic states typical for NIR transitions greatly accelerates excitation decay (*17*, *18*) and prevents both high brightness and polarization anisotropy. Furthermore, NIR CPL emitters based on low-bandgap semiconductors such as cadmium selenide (*19*) face additional challenges, including susceptibility to oxidation. Overcoming these limitations requires out-of-the-box approaches for chiral materials capable of photon emission.

Light emission anisotropy factors, such as g_{lum}, which characterizes the ellipticity of luminescence, and its counterpart, g_{em} (em, emission), quantifying the cumulative effect of luminescence and scattering, are the key metrics for CPL materials. Although rare earth complexes exhibit high g_{lum} between 0.1 and 1, arising from large spin-orbital coupling with *f*-electron states (*20*, *21*), typical anisotropy factor values for Earth-abundant materials range between 10^{-5} and 10^{-2}. Materials intended for use in visible light-emitting devices necessitate g_{em} values between 0.1 and 1.9 (*8*, *22*, *23*). By contrast, materials targeted for applications in the NIR region exhibit even smaller values of g_{em} and luminescence quantum yields. Rapid thermal relaxation rates and stringent symmetry restrictions exacerbate the problem, typically rendering them CPL-inactive.

Aerial brightness represents another crucial parameter for chiral materials and CPL emitters. Although plasmonic nanostructures offer promising optical polarizations, they are associated with high optical losses. The typical brightness values for them in the visible region (*24*, *25*) are in the range of 10^{-7} to 10^{-2} W/cm^2 (fig. S1 and table S1), and comparable data for NIR CPL emitters have not been reported.

Black-body radiation (BBR) offers an alternative to the challenges posed by closely spaced vibronic levels. All quantum states, even those separated by subelectron-volt gaps, are BBR-active in accordance with Planck's law. However, the same law does not account for polarization effects, considering them insignificant—which is true for a large spherical body typically considered in the framework of this law. Furthermore, the fluctuation-dissipation theorem specifically prohibits the generation of circularly polarized BBR (CP-BBR) from two-dimensional (2D) emitters (*26*), a geometry commonly used in light-emitting devices and previous CPL-emitter implementations. We hypothesized that 3D twisted filaments could serve as strong CPL-active BBR emitters because the overall mirror asymmetry of the emitter at nanometer and submicron scales—rather than the asymmetry of quantum states—would determine the circular polarization of thermal radiation. We report that twisted filaments composed of carbon nanotube (CNT) yarns, as well as twisted tungsten wires, generate CPL with exceptional brightness and high g_{em} values spanning the visible, NIR, and mid-infrared ranges. The filaments' helical geometry, the simplicity of their manufacturing, and their electrically controlled emission maximum enable the tunability of BBR-based CPL emitters.

Materials engineering of CP-BBR emitters

Planck's law provides a theoretical foundation for understanding the frequency and temperature dependence of BBR. However, BBR-based CPL emitters necessitate engineering chiral materials that can withstand high temperatures. In this regard, CNTs have high-temperature resistance that enables operation at >1000°C, and their fibrillar morphology renders them ideal candidates for filaments with nanoscale-to-microscale chirality, comparable in scale to the wavelengths of visible and infrared photons. Thus, we twisted CNT yarns with a diameter (D) of 150 μm into helical filaments with both left- and right-handedness (Fig. 1, B to D). Unlike molecular CPL emitters, their pitch (p) could be continuously varied from 1600 to 300 μm by gradual twisting. The nanofiber twist angles (β) can be varied from –40° to 40°, corresponding to right-handed (RH) and left-handed (LH) filaments, respectively.

We exploited the electrical conductivity of CNTs to generate BBR through resistive heating (*27*, *28*), which is convenient for voltage-controlled "tuning" of emission wavelength and intensity (Fig. 1, A and E, and figs. S2 and S3). The filaments emitted red light at 4 V and became visibly brilliant at 7 V, with radiation temperature reaching 1200°C. BBR from the twisted filaments displayed ellipticity determined by their chirality and applied voltages (fig. S4). RH filaments displayed LH ellipticity and vice versa for the filaments with opposite chirality (Fig. 1F). Circular anisotropy g factor was calculated as $g_{em} = \frac{2 \times I_{CP\text{-}BBR}}{I_{LCP} + I_{RCP}}$, where $I_{CP\text{-}BBR} = I_{LCP} - I_{RCP}$, and I_{LCP} and I_{RCP} correspond to the intensities of LH and RH CPL components from the thermal emission. When operating at 7 V, the maxima of g_{em} spectra reached 0.02 (for ~700 nm) and 0.06 (for ~1300 nm), exceeding those of comparable CPL emitters by factors of 10 to 10^4 (*22*, *23*). The brightness of the CP-BBR under the same conditions was 9.1 W/cm^2, surpassing those of photo- and electroluminescent CPL emitters in both the visible (*24*, *29*) and infrared (*30*, *31*) ranges by factors of 20 to 10^7 (table S1). Owing to spectral proximity

[1]Center for Complex Particle Systems (COMPASS), University of Michigan, Ann Arbor, MI, USA. [2]Department of Chemical Engineering, University of Michigan, Ann Arbor, MI, USA. [3]Biointerfaces Institute, University of Michigan, Ann Arbor, MI, USA. [4]Department of Chemical and Biological Engineering, Rensselaer Polytechnic Institute, Troy, NY, USA. [5]Department of Materials Science and Engineering, University of Michigan, Ann Arbor, MI, USA.
*Corresponding author. Email: kotov@umich.edu (N.A.K.)

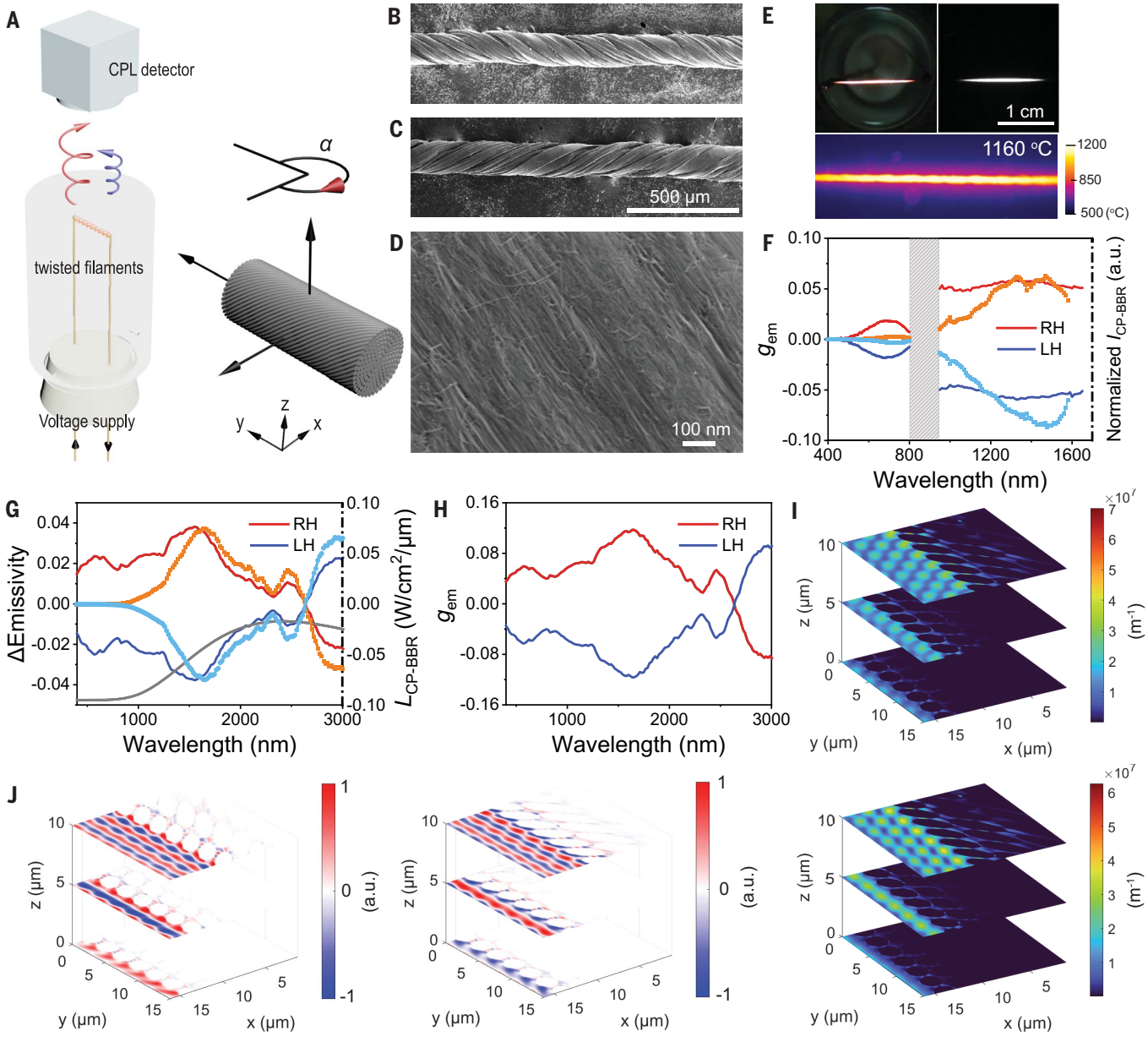

Fig. 1. Circularly polarized BBR of twisted filaments. (**A**) Schematics of the CP-BBR of twisted CNT filaments recorded by a CPL detector. The filament was initially placed along the *y* axis and rotated clockwise in the *x*-*y* plane with an angle variation of α in relation to its original position. (**B** to **D**) Scanning electron microscope (SEM) images at different magnifications for RH [(B) and (D)] and LH (C) CNT filaments. (**E**) Photographs of CNT filaments under visible (top left), NIR (top right), and infrared (bottom) cameras with a working voltage of 7 V. (**F** to **H**) Comparison of experimentally measured (F) and FDTD-calculated [(G) and (H)] non-angle-relevant LCP/RCP emissivity difference (G), CP-BBR [(F) and (G)], and g_{em} [(F) and (H)] spectra averaged over α from 0° to 360° for LH and RH filaments. The spectroscopic gap from 800 to 950 nm shown in (F) is caused by limitations of the currently available instruments for the circular polarization measurements and the need to utilize two different spectrometers that leave this gap in between. The gray line in (G) shows the ideal BBR spectra $\left[L_{\gamma=1}(\omega, T)\right]$ from Planck's law. (**I** and **J**) Local emissivity density (I) of LCP (top) and RCP (bottom) radiation for a RH filament, based on Kirchhoff's law; corresponding distribution of local spin angular momentum density of *z* components for LH (left) and RH (right) filaments.

maxima for emissivity and high Planck's radiance, the total electrical-to-optical conversion efficiency reached ~15% (fig. S2D and supplementary text 3). The filaments with voltages <5.5 V were operational for up to ~120 hours (figs. S3B and S5).

Mechanism of CP-BBR

Although the studies of BBR polarization from resistively heated filaments could have been a topic of interest since Planck, the actual investigations in this area are surprisingly limited (*31*–*35*). Kirchhoff's law of thermal radiation (*36*) establishes the equality between the emissivity and absorptivity of thermal emitters (*37*–*39*), representing the fundamental reason for BBR from twisted nanostructured materials being circularly polarized. It also provides a pathway to model CP-BBR by using finite-difference time-domain

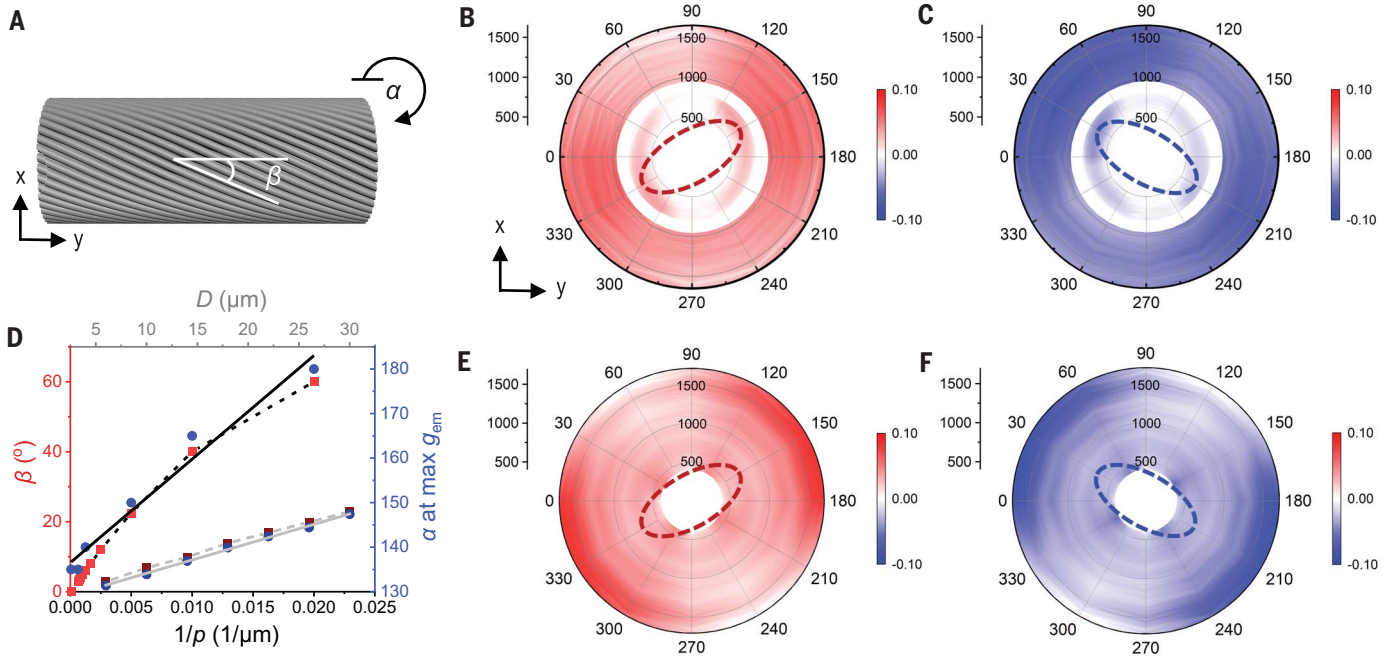

Fig. 2. Angular distribution of CP-BBR. (**A**) Illustration of a RH filament with a nanofiber twist angle, β. (**B**, **C**, **E**, and **F**) Comparison of experimentally measured [(B) and (C)] and FDTD-calculated [(E) and (F)] angular distribution maps of g_{em} with α for RH [(B) and (E)] and LH [(C) and (F)] filaments under 0° < α < 360°. (**D**) Dependence of β and α with maximum g_{em} in the angular distribution maps for filaments with various pitches, *p*, and diameters, *D*.

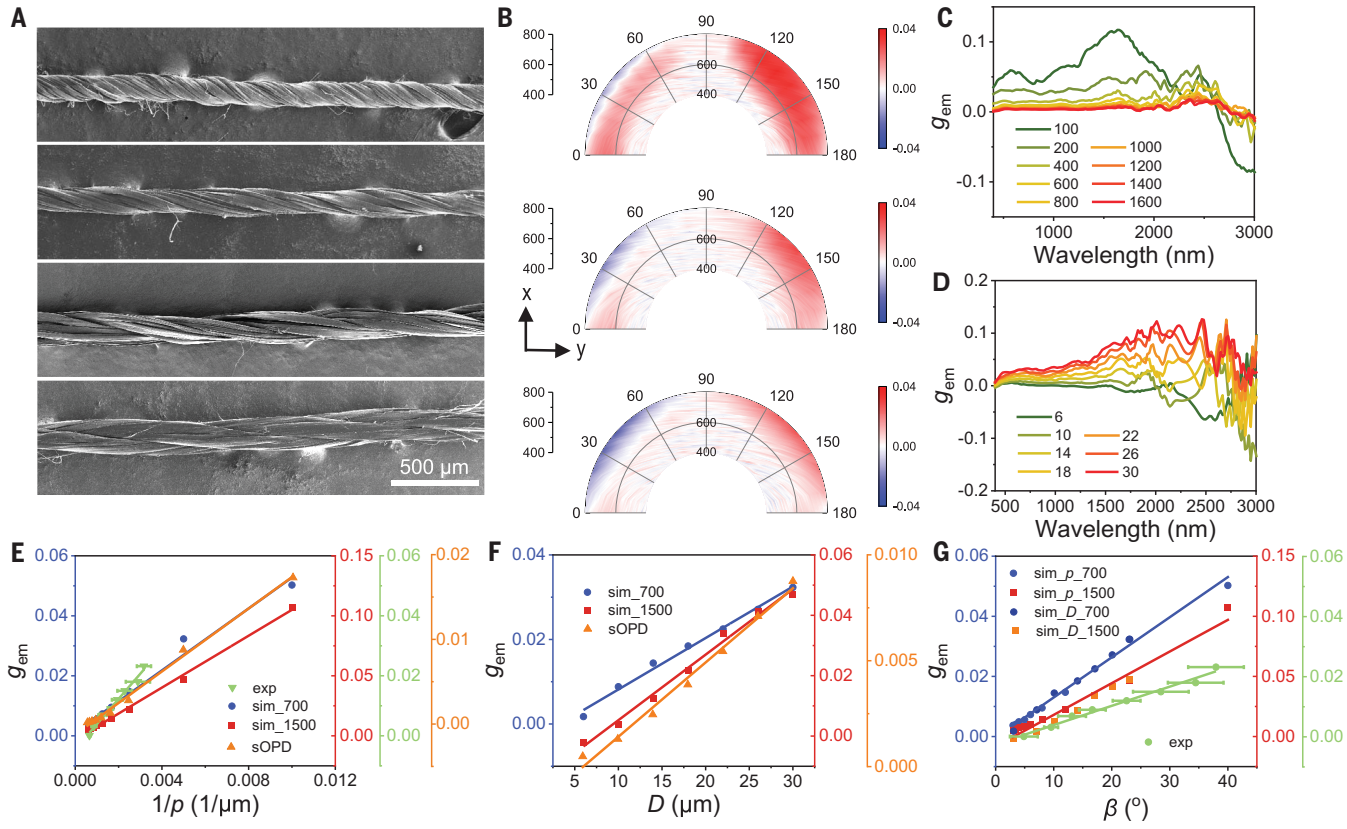

Fig. 3. Tunability of circular polarization by geometrical parameters. (**A**) SEM images of RH CNT filaments with *p* of 320 ± 30, 620 ± 40, 1200 ± 150, and 1600 ± 130 μm (from top to bottom). (**B**) Angular distribution maps of g_{em} for the filaments with *p* of 320 (top), 620 (middle), and 1200 (bottom) μm under 0° ≤ α < 180°. (**C** and **D**) FDTD-calculated g_{em} spectra for RH CNT filaments with various *p* (C) and *D* (D). (**E** and **F**) Dependence of g_{em} and scaled Osipov-Pickup-Dunmur chirality measure, based on the values of *p* (E) and *D* (F) of used filaments. (**G**) Dependence of g_{em} on β for the twisted filaments with different geometries. Error bars correspond to standard deviation based on the count of the helical turns of whole filaments.

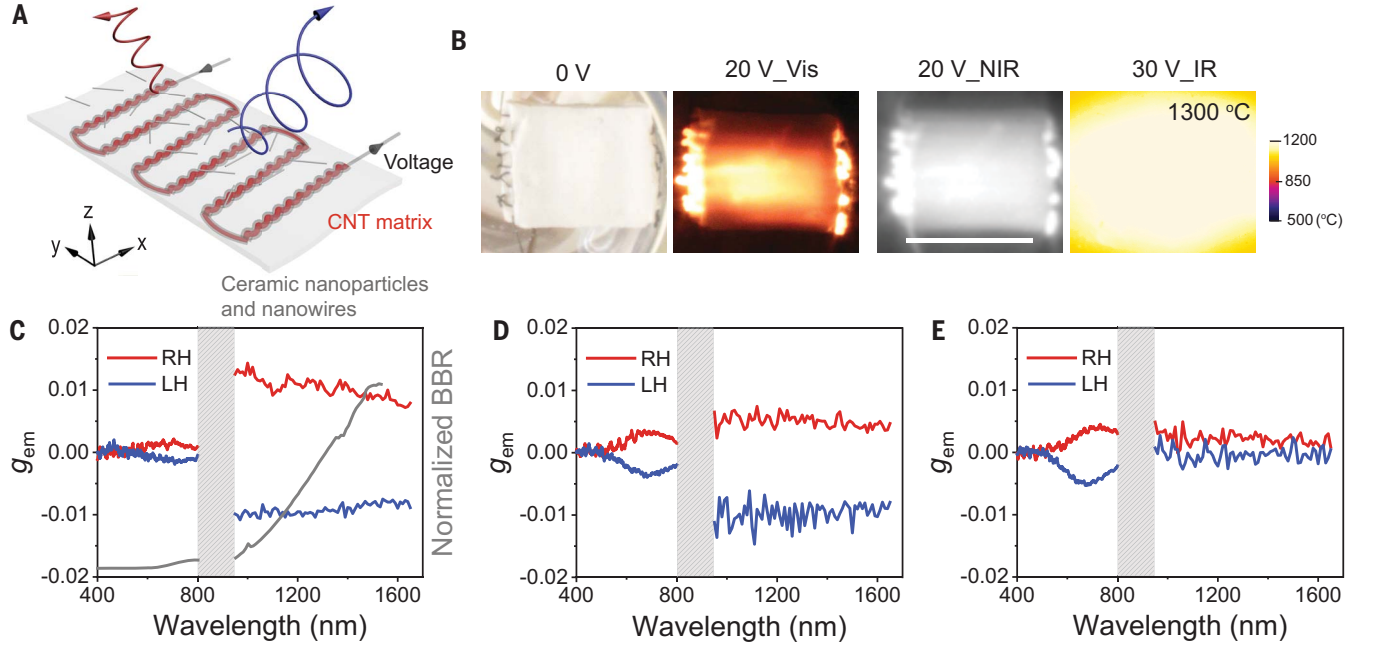

Fig. 4. Ultrahigh-temperature composites with CP-BBR. (**A**) Illustration for the structure of ultrahigh-temperature composites consisting of twisted CNT filaments, ceramic nanoparticles, and nanowires under electrical charging. (**B**) Photographs of the CNT-Al_2O_3 composite under visible, NIR, and infrared cameras. Scale bar, 1 cm. (**C** to **E**) g_{em} spectra averaged for α from 0° to 360° for the CNT-Al_2O_3 (C), CNT-SiO_2 (D), and CNT-ZrO_2 (E) composites with matrices of LH and RH CNT filaments.

(FDTD) computations. The BBR spectral radiance can be expressed as $L_{BBR}(\omega, T) = \gamma(\omega, T) \times L_{\gamma=1}(\omega, T)$ (*39*, *40*), where γ is the far-field emissivity of black bodies, ω and T are the photon frequency and body temperature, and $L_{\gamma=1}(\omega, T)$ is the radiance of an ideal black body with an emissivity of γ = 1. g_{em}, L_{LCP}, L_{RCP}, γ_{LCP}, and γ_{RCP} are related as $g_{em} = \frac{2 \times I_{CP-BBR}}{I_{LCP} + I_{RCP}} = \frac{2 \times L_{CP-BBR}}{L_{LCP} + L_{RCP}} = \frac{2 \times (\gamma_{LCP} - \gamma_{RCP})}{\gamma_{LCP} + \gamma_{RCP}}$. We obtained $L_{\gamma=1}(\omega, T)$ according to Planck's law, whereas the emissivity was calculated with FDTD on the basis of its equality with absorptivity under flux photon with frequency ω. All the experimental data obtained for 400 to 800 nm and 950 to 1650 nm matched the calculated spectra (Fig. 1, F to H, and figs. S6 and S7). As another benchmark for the validity of the proposed mechanism, the far-field ellipticity from filaments can be treated as a superposition of local emitters with $\gamma_{local}(\omega, p') = \mathrm{Im}[\varepsilon(\omega, p')] \cdot [\omega |E(\omega, p')|^2] / [c |E_0(\omega, p')|^2]$, where $\varepsilon(\omega, p')$ is the dielectric permittivity at point p', and E and E_0 are the local electrical fields under incident LCP and RCP beams propagating along the z axis. Integration of local emissivities $\gamma_{local}(\omega, p')$ for RH filaments indicates that far-field emissions are dominated by the ellipticity of LH photons, which is consistent with spectrum calculations and experimental observations (Fig. 1, F to I).

Spin angular momentum (S) density of emitted photons can be calculated from the local- and far-field regions of electric and magnetic (H) fields as $S = \frac{1}{4\omega} \mathrm{Im}(\varepsilon_0 E^* \times E + \mu_0 H^* \times H)$ (*41*, *42*), where ε_0 and μ_0 are the permittivity and permeability of free space. For an achiral filament, the net S = 0 along any axis. But for twisted filaments, the net S was dependent on the radial distance from the filament and the position along the y axis following the twisted geometry of the filament. In the x-y plane, the x and y components of S, S_x, and S_y cancel each other, but the z components $S_z \neq 0$, leading to the circular polarization of BBR (Fig. 1J and fig. S8). This finding and the spatial maps of S give the direct evidence that circular polarization originates from the 3D submicroscale geometry of filaments rather than from quantum states. Additionally, we also tested for potential contributions from current-induced magnetic field effects due to passing current, but they are clearly negligible (fig. S9).

Angle dependence of CP-BBR from twisted filaments

BBR was isotropic and omnidirectional in the x-z plane for the filaments aligned along the y axis (figs. S10 to S12). By contrast, the degrees of linear and circular polarization of BBR in the x-y plane were strongly anisotropic. Linear polarization was aligned perpendicular to the filaments for achiral nanostructures, whereas the superposition of local chiral emitters in twisted filaments resulted in polarization maxima slightly misaligned with the filament axis.

Conforming to the mechanism of CP-BBR described above, the degree of circular polarization was determined by the twist angle β representative of helicity of filaments (Fig. 2A). Circular polarization anisotropy was also dependent on the filament orientation (Fig. 2, A to C, and figs. S13 and S14). The RH and LH filaments exhibited perfectly mirrored angular distribution patterns, with maximum g_{em} = 0.08 at α = 150° and α = 30°. FDTD calculations based on Kirchhoff's law fully reproduced experimental observations (Fig. 2, E and F).

We anticipated that the angular distribution patterns would change for different values of p and D. Indeed, a near-linear dependence of twist angle β with $1/p$ and D was observed (Fig. 2D), and the angular distribution maps of g_{em} changed with β. For achiral filaments, i.e., β = 0°, the filaments exhibited crossed and mirrored polarization patterns, with a maximum g_{em} observed at α = 135° and α = 45° for LCP and RCP radiation. As β increased, the crossed pattern gradually transitioned into a monopolar pattern owing to the emergence of net circular polarization effects. The angle corresponding to the g_{em} maximum, determined by the linear polarization directions and β, rotated toward 180° and 0° for RH and LH filaments (Fig. 2D and figs. S11, S12, S15, and S16). The value of α for g_{em} maximum also exhibited a linear dependence on $1/p$ and D, establishing a solid foundation for the design of CP-BBR emitters.

All the circular polarization effects and angular distribution maps were replicated with

twisted tungsten filaments (fig. S17), confirming the generality of the observed phenomena as required by Planck's law. Optical asymmetry g_{em} spectra of twisted tungsten filaments and angular distribution patterns were nearly identical to those of CNT filaments with similar β values, exhibiting g_{em} maxima at $\alpha = 150°$ and $\alpha = 30°$ for LCP and RCP radiations.

Helicity dependence of CP-BBR of the twisted filaments

We experimentally varied β between 7° and 35° and p from 1600 to 300 μm by changing the tightness of twist in the filaments (Fig. 3A and table S2). Linear dependencies of g_{em} on $1/p$, β (Fig. 3, B, C, E, and G, and figs. S18 and S19), and filament diameter (Fig. 3, D, F, and G, and fig. S20) were observed. For large values of $p = 1200 \pm 150$ μm and $\beta = 11 \pm 1°$, the g_{em} was expectedly small. For small values of $p = 320 \pm 30$ μm, corresponding to $\beta = 35 \pm 4°$, the intensity of CP-BBR rose dramatically. We found that g_{em} did not change the sign for any α, which is essential for practical CPL emitters. All the dependencies were reproduced in simulations that are based on the proposed mechanism of CP-BBR (Fig. 3, E to G).

Additional insights into the relation between the mirror asymmetry of the filaments and g_{em} were revealed by calculating the optical chirality density (C) (*43*) and scaled Osipov-Pickup-Dunmur (sOPD) chirality measure. A linear correlation of C with g_{em} according to Kirchhoff's law was confirmed on the basis of the near-field C distributions for filaments with different geometric parameters (figs. S19 and S20). The utility of chirality measures has been previously questioned (*44*), which is especially warranted for OPD and other pseudoscalar (i.e., bisignate) measures that can generate so called "chiral zeros"—the mirror asymmetric point sets with chirality measure equal to zero. However, for a set of chiral geometries with a defined reconfiguration path that definitively passes through a "flat" achiral state, the pseudoscalar measures do not reveal "chiral zeros," and their values adequately quantify the mirror asymmetry of twisted filaments. Indeed, we observed that sOPD has a linear dependence on $1/p$, D, and g_{em} (Fig. 3, E and F, and fig. S21). In this specific case, this relation is due to left-to-right reconfiguration passing through highly symmetrical cylindrical geometry with zero chirality (*45*), which is true for every helicoid. Thus, the design of CP-BBR emitters that maximize g_{em} can be based on this geometrical parameter that directly impacts the ellipticity of BBR.

Refractive composites with CP-BBR

Resistive heating to high temperatures and cylindrical form factor of the twisted filaments will limit applications of CP-BBR in consumer electronics. But none of the current CPL emitters can operate at high temperatures. At moderately elevated temperatures between 50 and 200°C, the brightness and g_{em} of small molecules, molecular crystals, organic polymers, and inorganic nanoparticles plummet owing to the activation of additional thermalization pathways of excited states (*46*–*48*). At temperatures >200°C, all current CPL materials decompose.

To demonstrate a variable form factor and to create CP-BBR emitters taking advantage of high temperatures, we sintered achiral ceramic nanoparticles with twisted CNT filaments arranged in a snake-like fashion (Fig. 4A). The carbon-ceramic composites obtained by sintering Al_2O_3 nanoparticles with twisted nanocarbon filaments withstood temperatures ~1300°C and exhibited strong CPL (Fig. 4B). As with the case for individual filaments, the polarization rotation was opposite for LH and RH fibers embedded into the composites. The directional asymmetry polarized emission was also reduced, revealing angle-independent $g_{em} = 0.01$ in the NIR range (Fig. 4C and fig. S22). Other refractive composites made from SiO_2 and ZrO_2 displayed similar characteristics, with small changes in g_{em} caused by variations in the refractive index of the ceramic matrix (Fig. 4, D and E).

Conclusions

Emitters with high brightness and strong polarization rotation spanning visible, NIR, and infrared parts of the spectrum have been designed and realized, taking advantage of the equality with absorptivity determined by the submicron-scale chirality of the black body. A thoroughly verified CP-BBR mechanism leads to high predictability of the spectral characteristics and to engineering simplicity of CP-BBR emitters. Sintering twisted filaments with ceramic nanoparticles opens a door to a large family of chiral carbon-ceramic composites. These materials can impart CPL emissivity to a wide range of high-temperature objects and provide a materials platform for CPL emitters in extreme conditions inaccessible to current chiral materials.

REFERENCES AND NOTES

1. J. Lu *et al*., *Science* **371**, 1368–1374 (2021).
2. H.-E. Lee *et al*., *Nature* **556**, 360–365 (2018).
3. X. Zhang, Y. Liu, J. Han, Y. Kivshar, Q. Song, *Science* **377**, 1215–1218 (2022).
4. Y. Kim *et al*., *Adv. Mater.* **32**, e2003051 (2020).
5. L. A. Warning *et al*., *ACS Nano* **15**, 15538–15566 (2021).
6. F. Furlan *et al*., *Nat. Photonics* **18**, 658–668 (2024).
7. D.-W. Zhang, M. Li, C.-F. Chen, *Chem. Soc. Rev.* **49**, 1331–1343 (2020).
8. H. He *et al*., *Laser Photonics Rev.* **16**, 2200115 (2022).
9. S. Liu *et al*., *Matter* **5**, 2319–2333 (2022).
10. C. Guo, F. Liu, S. Chen, C. Feng, Z. Zeng, *IEEE Commun. Surv. Tutor.* **19**, 125–166 (2017).
11. X. Fang, H. Ren, M. Gu, *Nat. Photonics* **14**, 102–108 (2020).
12. M. Toyoshima *et al*., *Opt. Express* **17**, 22333–22340 (2009).
13. D. N. Neshev, A. E. Miroshnichenko, *Nat. Photonics* **17**, 26–35 (2023).
14. A. Orieux, E. Diamanti, *J. Opt.* **18**, 083002 (2016).
15. C. He *et al*., *Light Sci. Appl.* **10**, 194 (2021).
16. R. Gao, L. Xu, C. Hao, C. Xu, H. Kuang, *Angew. Chem. Int. Ed.* **58**, 3913–3917 (2019).
17. R. Englman, J. Jortner, *Mol. Phys.* **18**, 145–164 (1970).
18. M. Bixon, J. Jortner, J. Cortes, H. Heitele, M. E. Michel-Beyerle, *J. Phys. Chem.* **98**, 7289–7299 (1994).
19. Z. Ni *et al*., *ACS Nano* **17**, 20611–20620 (2023).
20. O. G. Willis, A. Pucci, E. Cavalli, F. Zinna, L. Di Bari, *J. Mater. Chem. C Mater. Opt. Electron. Devices* **11**, 5290–5296 (2023).
21. N. F. M. Mukthar, N. D. Schley, G. Ung, *J. Am. Chem. Soc.* **144**, 6148–6153 (2022).
22. J. Lv, X. Yang, Z. Tang, *Adv. Mater.* **35**, e2209539 (2023).
23. S. Jiang, N. A. Kotov, *Adv. Mater.* **35**, e2108431 (2023).
24. L. Wan *et al*., *ACS Appl. Mater. Interfaces* **12**, 39471–39478 (2020).
25. T.-Y. Li *et al*., *Sci. Rep.* **5**, 14912 (2015).
26. S. L. Wadsworth, P. G. Clem, E. D. Branson, G. D. Boreman, *Opt. Mater. Express* **1**, 466–479 (2011).
27. P. Li *et al*., *Appl. Phys. Lett.* **82**, 1763–1765 (2003).
28. Y. Sun *et al*., *Adv. Eng. Mater.* **21**, 1801126 (2019).
29. Z. Chen *et al*., *Adv. Mater.* **34**, e2109147 (2022).
30. X. Wang *et al*., *Sci. Adv.* **9**, eade4203 (2023).
31. A. Nguyen *et al*., *Optica* **10**, 232–238 (2023).
32. A. C. Overvig, S. A. Mann, A. Alù, *Phys. Rev. X* **11**, 021050 (2021).
33. C. Wu *et al*., *Nat. Commun.* **5**, 3892 (2014).
34. J. C. W. Lee, C. T. Chan, *Appl. Phys. Lett.* **90**, 051912 (2007).
35. C. Khandekar, Z. Jacob, *Phys. Rev. Appl.* **12**, 014053 (2019).
36. G. Kirchhoff, *Ann. Phys.* **185**, 275–301 (1860).
37. P. Robitaille, *Prog. Phys.* **4**, 3–13 (2009).
38. P. Robitaille, *IEEE Trans. Plasma Sci.* **31**, 1263–1267 (2003).
39. D. G. Baranov *et al*., *Nat. Mater.* **18**, 920–930 (2019).
40. Y. Li *et al*., *Nat. Rev. Mater.* **6**, 488–507 (2021).
41. M. Neugebauer, J. S. Eismann, T. Bauer, P. Banzer, *Phys. Rev. X* **8**, 021042 (2018).
42. M. Neugebauer, T. Bauer, A. Aiello, P. Banzer, *Phys. Rev. Lett.* **114**, 063901 (2015).
43. Y. Tang, A. E. Cohen, *Phys. Rev. Lett.* **104**, 163901 (2010).
44. M. Petitjean, *Entropy (Basel)* **5**, 271–312 (2003).
45. P. Kumar *et al*., *Nature* **615**, 418–424 (2023).
46. J. Lu *et al*., *Nature* **630**, 860–865 (2024).
47. W. Yan, S. Li, Y. Zhang, Q. Yao, S. D. Tse, *J. Phys. Chem. C Nanomater. Interfaces* **114**, 10755–10760 (2010).
48. T. Kosaka, S. Iwai, Y. Inoue, T. Moriuchi, T. Mori, *J. Phys. Chem. A* **122**, 7455–7463 (2018).

ACKNOWLEDGMENTS

We thank the Michigan Center for Materials Characterization [$(MC)^2$] for instrument support. **Funding:** This work was supported in part by the Vannevar Bush DoD Fellowship to N.A.K. titled "Engineered Chiral Ceramics" [Office of Naval Research (ONR), grant N000141812876], in part by the "Center of Complex Particle Systems (COMPASS)" (grant NSF 2243104), and by the ONR MURI project "Mechanics or Metamaterials" (grant N00014-20-1-2479), ONR COVID-19 Newton Award "Pathways to Complexity with 'Imperfect' Nanoparticles" (grant HQ00342010033), and Air Force Office of Scientific Research grant "Graph Theory Description of Network Material" (grant AFOSR FA9550-20-1-0265). **Author contributions:** J.L. and N.A.K. designed and performed the experiments, FDTD simulations, optical chirality calculations, and data analysis. H.J.J. and J.L. fabricated the high-temperature composites and studied their optical activities. J.-Y.K. ran the OPD calculations. All the authors contributed to the writing of the paper. N.A.K. conceived and supervised the project. **Competing interests:** The authors declare that they have no competing interests. **Data and materials availability:** All data are available in the main text or the supplementary materials.

SUPPLEMENTARY MATERIALS

science.org/doi/10.1126/science.adq4068
Materials and Methods
Supplementary Text
Figs. S1 to S22
Tables S1 and S2
References (*49*–*77*)

Submitted 12 May 2024; accepted 5 September 2024
10.1126/science.adq4068